# Novel ternary core-shell structure with microwave absorption properties and low infrared emissivity

Chunhao Wan [a,1], Rong Yan [a,1], Shansheng Yu [a], Xiaoyi Wang [b,**], Hongwei Tian [a,*]

[a] *Key Laboratory of Automobile Materials of MOE and School of Materials Science and Engineering, Jilin University, Changchun, 130012, China*
[b] *Key Laboratory of Optical System Advanced Manufacturing Technology, Changchun Institute of Optics, Fine Mechanics and Physics, Chinese Academy of Sciences, Changchun, 130033, China*

## ARTICLE INFO

## ABSTRACT

The development of functional materials with dual characteristics of microwave absorption and low infrared emissivity is vital for protection against magnetic-wave contamination. Currently, both microwave protection and infrared protection technologies are developing rapidly, but simultaneous integration of both has not been extensively investigated. Herein, a new ternary core-shell $CoFe_2O_4@SiO_2@ZAO$ composite dual-functional material was designed and fabricated. The process consisted of coating $CoFe_2O_4$ microspheres with ZAO based on $SiO_2$ middle layer prepared through hydrolysis and sol-gel methods. The introduction of ZAO and $SiO_2$ was found conducive to dielectric loss and impedance matching, thereby improving wave absorption. The nano-flower ZAO coating provided low infrared emissivity with a lamellar structure and high carrier concentration in the resulting ternary structure. The rise in ZAO content first enhanced the wave absorption of $CoFe_2O_4@SiO_2@ZAO$ and then decreased while the infrared emissivity declined. Among prepared samples, $CoFe_2O_4@SiO_2@ZAO$ exhibited a minimum reflection loss ($RL_{min}$) of −59.31 dB at 10.96 GHz, conducive to effective absorption bandwidth (EAB) of 4 GHz at 2 mm thickness with an infrared emissivity of 0.71 in 8–14 μm waveband. In sum, the novel $CoFe_2O_4@SiO_2@ZAO$ core-shell structure showed attractive properties in terms of compatibility of wave absorption and infrared emissivity, promising for future syntheses of dual-functional materials with improved performance.

## 1. Introduction

Dual-function materials with low infrared emissivity and enhanced microwave absorption are vital for many applications [1–6]. In principle, the radar and infrared stealth are intrinsically opposite. Radar detection is to receive the reflection wave generated by microwaves reaching the surface. Wave absorption materials for radar stealth with high absorption and low reflection attenuate electromagnetic waves between 2 and 18 GHz via loss mechanisms [7,8]. In contrast, the principle of infrared detection is to convert the characteristic signal of infrared radiation into an electrical signal through the infrared photoelectric effect, which is generated by the photon energy from the infrared radiation. The infrared stealthy materials are required for low absorption and high reflection at 3–5 and 8–14 μm [9]. Therefore, studying the two opposite stealth mechanisms remains very challenging

[10–14]. Two primary dual-function methods exist: i) composite coating and ii) composite materials. The composite coating method possesses two or more single-function layers with a surface consisting of a low infrared emissivity layer with better microwave transmission as a filter, and an inner layer close to the substrate characterized by microwave absorption. Nevertheless, compound coating with both weight gain and impedance mismatch results in performance degradation of wave absorption and infrared emissivity. In this view, Ma et al. [15] designed a metamaterial consisting of ITO-coated-PET films and a polyvinyl chloride substrate. The film was composed of an infrared shielding layer, a radar absorption layer, a substrate, and a backplane with a total thickness of only 3.5 mm at waveband from 7.3 to 18.8 GHz and low infrared emissivity of 0.49. The composite materials method consists of combining dual-function materials by proper treatment. Liu et al. [16] fabricated $Al@MnO_2$ composites by anchoring $MnO_2$ nanoparticles on

---

\* Corresponding author.
\*\* Corresponding author.
  *E-mail addresses:* wangxiaoyi@163.com (X. Wang), tianhw@jlu.edu.cn (H. Tian).
  [1] Chunhao Wan and Rong Yan contributed equally to this work.

aluminum sheets through a facile one-step method to yield polarization effect and good impedance matching. The minimum reflection loss ($RL_{min}$) reached −42.93 dB at a thickness of 1.0 mm, while infrared emissivity reached 0.55 at the lowest band range of 8–14 μm. In general, composite materials are thinner and lighter than composite coatings, conducive to a simplified production process and ensuring properties homogeneity [17,18].

The low wave absorption in traditional structure materials requires the construction of flake-like structures with low infrared emissivity and multireflection space. Among structures, the core-shell structure possesses a large surface area and multi-component features as important features of dual-function materials [19–21]. In terms of wave absorption, the interface polarization from core shell structure would result in microwave attenuation. Accordingly, composites with core-shell structures can adjust permittivity and optimize impedance matching properties. In terms of low infrared emissivity, core-shell structures can also form conductive pathways in the composite for lower infrared emissivity. For that, core-shell structures could use the outer layer for low infrared emissivity and the inner layer for wave absorption following the double coating principle to achieve a dual function.

Among functional materials, $CoFe_2O_4$ shows excellent magnetic loss performance and stability, extensively exploited in wave absorption. The sphere morphology of $CoFe_2O_4$ has also been employed as the inner absorption layer. For example, Cheng et al. [22]prepared a carbon/-hollow $CoFe_2O_4$ biomimetic layered absorber with a minimum reflection loss of −53.54 dB at 2.46 mm, as well as a maximum effective absorption bandwidth (EAB) of 4.92 GHz at 1.7 mm. The strong absorption capacity of this material was attributed to the synthetic effect of conductive loss, magnetic loss, and dielectric loss. However, several underlying issues related to high conductivity, surface impedance mismatch, and high infrared emissivity induced by conductive loss were recorded.

ZAO is an N-type doped semiconductor possessing a low infrared emissivity, good impedance matching, and controllable morphology. In view of this, Rydzek et al. [23] prepared ZAO films by the sol-gel method on substrates followed by annealing to increase the number of carriers, resulting in reduced surface IR emissivity from 0.89 to less than 0.45, as well as retained good visible transmittance. Besides, the spectral characteristics and dielectric properties of ZAO can be altered by doping of Al [24,25]. Therefore, ZAO has enormous potential for use as an outer functional layer to improve the overall performance of semiconducting devices.

$SiO_2$ is a dielectric loss material, thereby can be used for wave absorption owing to its low reflection and high transmission able to maintain the overall absorption and infrared emissivity performance to greatly enrich the design of core-shell structures [26,27]. For instance, Wang et al. [28] reported $Co@SiO_2@Void@C$ yolk-shell composite with an $RL_{min}$ reaching −44.5 dB at 8.8 GHz for 1.7 mm combined with an EAB of 8.0 GHz. Accordingly, the middle layer consisting of $SiO_2$ connected to the magnetic core and carbon shell may significantly optimize impedance matching and shell adhesion. The presence of heterointerface and pores may also greatly contribute to microwave loss performance.

In general, the combination of $CoFe_2O_4$ and $SiO_2$ in wave absorption mechanism and the surface cladding of the low infrared emissivity ZAO enables core-shell structure materials to realize bifunctional behavior. Accordingly, novel $CoFe_2O_4@SiO_2@ZAO$ core-shell composites consisting of $CoFe_2O_4$ microsphere coated by $SiO_2$ middle layer followed by further coating by the varying contents of ZAO (Zn:Al = 93:7) were designed and fabricated according to reported hydrolysis and sol-gel methods. The morphologies of samples obtained at different ZAO contents, as well as the impacts of electromagnetic parameters on the properties of the resulting core-shell structure were all analyzed. The wave absorption and infrared emissivity characteristics of the resulting core-shell structures were compared and the best coating of dual function was determined. The data revealed that the gap of core-shell and

**Table 1**
Amounts of raw chemical reagents used to prepare different samples.

| Sample | $(CH_3COO)_2Zn·2H_2O$ (mg) | $Al(NO_3)_3·9H_2O$ (mg) | $C_2H_2O_4$ (mg) |
|---|---|---|---|
| S1 | 51.00 | 6.50 | 40 |
| S2 | 63.75 | 8.13 | 50 |
| S3 | 76.50 | 9.75 | 60 |
| S4 | 89.25 | 11.38 | 70 |

lamellar nanoflower greatly facilitated magnetic wave multi-reflection. Additionally, the large specific surface area enhanced interface polarization. The ternary composite combined the merits of magnetic loss and dielectric loss materials. $CoFe_2O_4$ provided hysteresis loss and residual loss, while $SiO_2$ as the basis of ZAO achieved electromagnetic wave transmission to the $CoFe_2O_4$ core. The coating of ZAO introduced more loss mechanisms and carriers, thereby improving the infrared emissivity and wave absorption. Overall, the strategy used to prepare $CoFe_2O_4@SiO_2@ZAO$ core-shell structure with optimized wave absorption and infrared emissivity looks promising for the future synthesis of dual-functional materials with improved performance.

## 2. Experimental

### 2.1. Materials

Cobalt(II) chloride hexahydrate ($CoCl_2·6H_2O$) was purchased from Xilong Scientific. Iron chloride hexahydrate ($FeCl_3·6H_2O$, 99.0%), zinc acetate dihydrate ($C_4H_6O_4Zn·2H_2O$, 99.0%), aluminum nitrate non-ahydrate ($Al(NO_3)_3·9H_2O$, 99.0%), and tetrapropyl orthosilicate (TPOS, 97%) were all obtained from Aladdin. Resorcinol ($C_6H_6O_2$, 99%), formaldehyde solution ($CH_2O$, 37.0 wt%), and polyethylene glycol 2000 (PEG-2000) were received from Macklin. Ammonia solution ($NH_3·H_2O$, 25.0 wt%), ethylene glycol (EG, 98%), and urea ($CH_4N_2O$, 99%) were all provided by Sinopharm. All chemicals were of AR grade and used as received without further purification. Deionized water used throughout the experiments was produced by an ultrapure water machine.

### 2.2. Preparation of CoFe2O4 nanospheres

$CoFe_2O_4$ nanospheres were synthesized by the hydrothermal process. Typically, $CoCl_2·6H_2O$ (928.65 mg), $FeCl_3·6H_2O$ (1688.25 mg), PEG-2000 (1000 mg), and urea (2800 mg) were first dispersed in EG (80 mL) under magnetic stirring for 2 h. The resulting solution was then transferred into a 150 mL Teflon reactor and heated in an oven at 190 °C for 12 h. After cooling down to room temperature, the obtained black powders were cleaned three times with deionized water and absolute ethanol before drying under vacuum at 45 °C for 20 h to yield $CoFe_2O_4$ microspheres.

### 2.3. Preparation of CoFe2O4@SiO2 nanospheres

The above as-prepared $CoFe_2O_4$ nanospheres (200 mg) were dispersed in mixed deionized water (80 mL) and absolute ethanol (15 mL) solution, subjected to ultrasonic treatment for 30 min, and then mechanical agitation to separate the spheres. $NH_3·H_2O$ (2 mL) and TPOS (0.5 mL) were then added to the mixture followed by stirring for 24 h at 30 °C and drying under vacuum at 45 °C for 12 h to yield $CoFe_2O_4@SiO_2$ microspheres.

### 2.4. Preparation of CoFe2O4@SiO2@ZAO nanospheres

The prepared $CoFe_2O_4@SiO_2$ was divided into 4 groups. Each group consisted of adding 100 mg into deionized water (50 mL) under ultrasonic dispersion for 30 min followed by continuous mechanical stirring. Different masses of $(CH_3COO)_2Zn·2H_2O$, $Al(NO_3)_3·9H_2O$ and $C_2H_2O_4$ were then added to the above solutions to yield solutions named S1, S2,
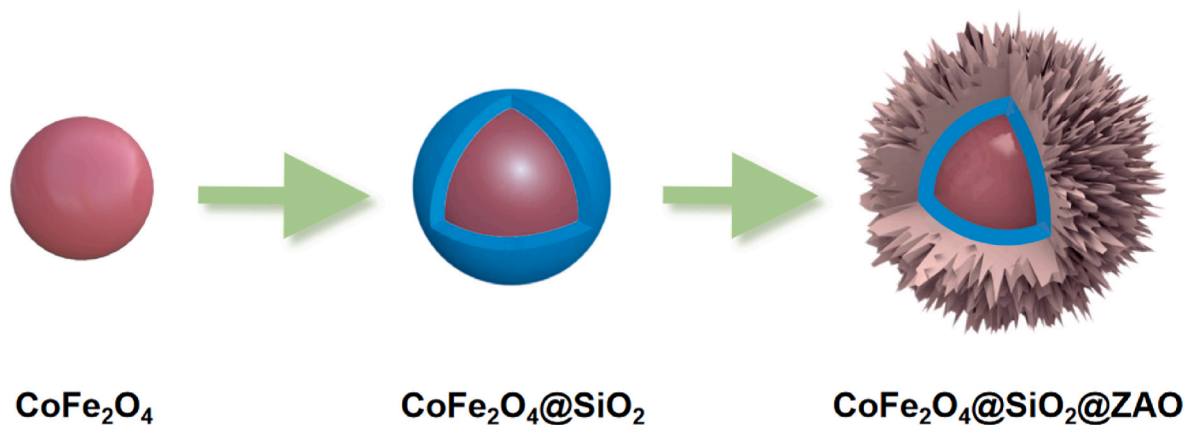
**Scheme 1.** The preparation process of CoFe$_2$O$_4$@SiO$_2$@ZAO core-shell structure.

S3, and S4 with the proportions listed in Table 1. Next, the solutions were heated and stirred in a water bath at 80 °C for 6 h. The mixtures were washed three times with anhydrous ethanol and deionized water, and dried under vacuum at 45 °C for 12 h. They were then fully ground followed by carbonization in a tube furnace filled with Ar at 200 °C (2 °C·min$^{-1}$) for 2 h to yield CoFe$_2$O$_4$@SiO$_2$@ZAO. The preparation process of CoFe$_2$O$_4$@SiO$_2$@ZAO is shown in Scheme 1.

### 2.5. Characterization

The crystalline structures and phase compositions of the samples were analyzed by X-ray diffraction (XRD, Bruker, D8 Advance) with Cu Kα radiation (λ = 1.5406 Å). The morphologies and particle sizes were characterized by scanning electron microscopy (SEM, Hitachi SU8010) and transmission electron microscopy (TEM, JEOL-2100F) equipped with an energy-dispersive spectroscopy (EDS) module. The surface components and chemical bonds were determined by X-ray

photoelectron spectroscopy (XPS, Escalab-250 X-ray). The Raman spectra were recorded on a Raman spectrometer (alpha-300R, Witec) at a laser excitation of 532 nm. Fourier transforms infrared (FT-IR) spectrometry was carried out on Thermo Scientific Nicolet iS20 equipment. The Brunauer–Emmett–Teller (BET) surface areas were measured by a TriStar II 3020, Micromeritics Instrument Corporation. Barret–Joyner–Halenda (BJH) pore size distribution was calculated from the absorption isotherms using nonlocal density functional theory. The magnetic properties were studied by means of a magnetic measurement system (VSM, Lakeshore7407). S3 with the best overall performance was selected for EDS, XPS, BJH, and BET characterization.

### 2.6. Measurement of electromagnetic parameters

The process consisted of first grounding the samples into fine powders followed by mixing with paraffin at a mass ratio of (40 wt% samples, 60 wt% paraffin). The obtained powders were then pressed in a
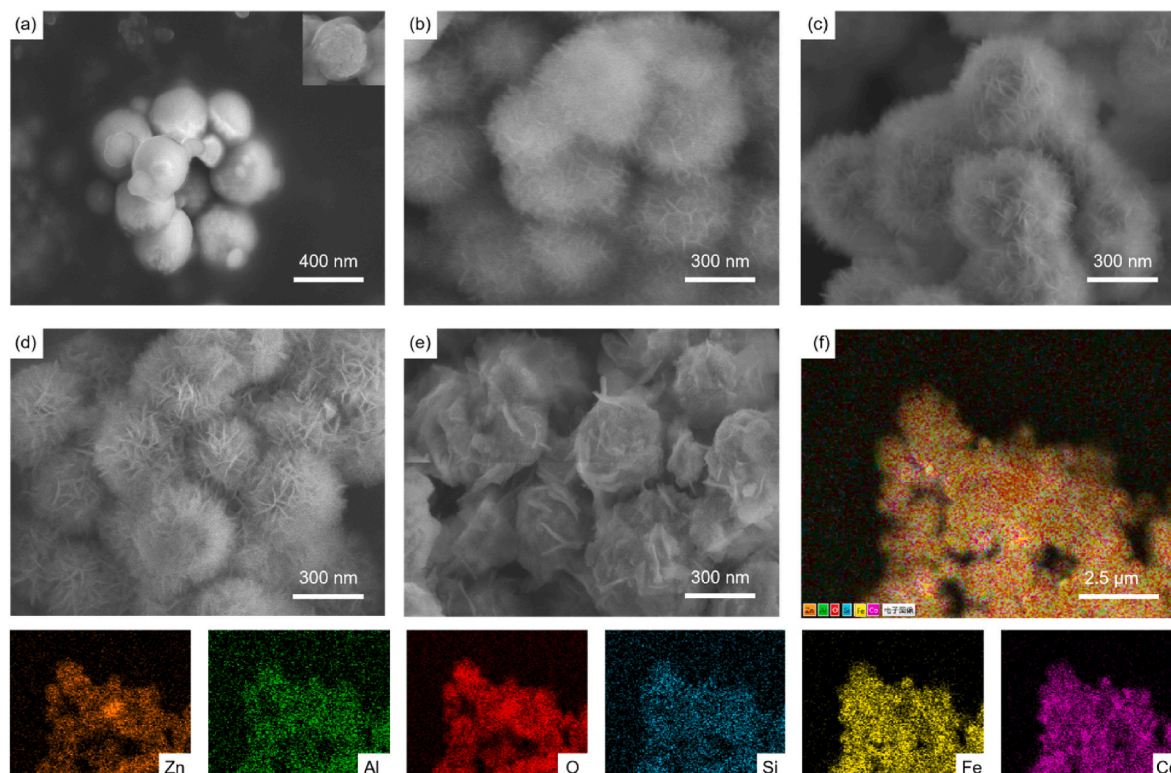


**Fig. 1.** SEM images of (a) CoFe$_2$O$_4$@SiO$_2$, (b) S1, (c) S2, (d) S3, (e) and S4. (f) EDS mapping of S3.
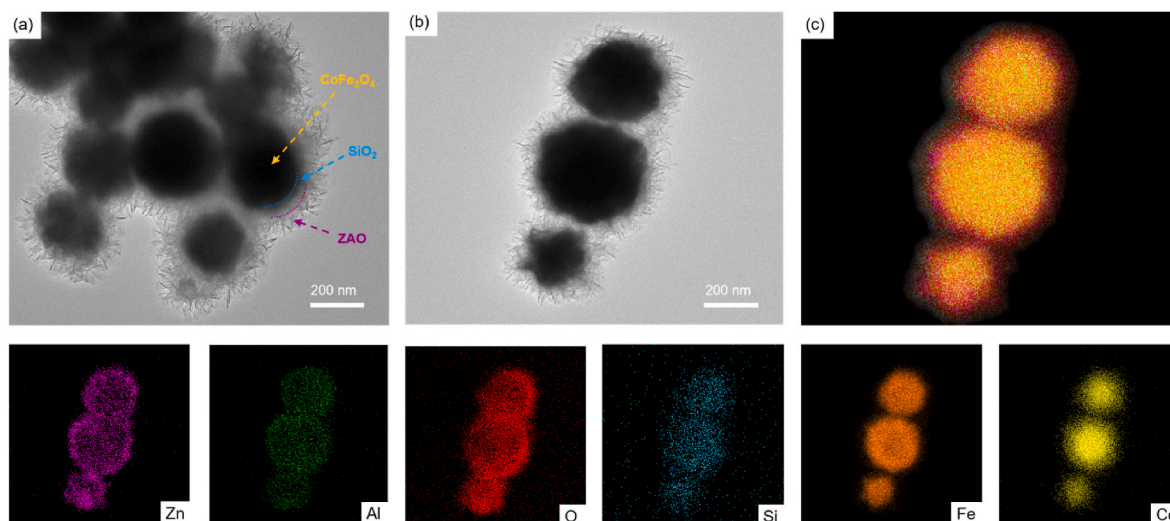
**Fig. 2.** (a, b) TEM images of S3. (c) EDS mapping of S3.

specific mold to form coaxial rings with an outer diameter of 6.95 mm and an inner diameter of 3.05 mm. The complex permittivity ($\varepsilon_r = \varepsilon' - j\varepsilon''$) and permeability ($\mu_r = \mu' - j\mu''$) of each composite were evaluated by a vector network analyzer (VNA, Agilent N5244A) in the range of 2–18 GHz.

### 2.7. Measurement of infrared emissivity

The average infrared emissivity was measured by an IR-II dual-band infrared emissometer in the 8–14 μm waveband after tableting. Fourier transforms infrared (FT-IR) spectrometry was used for measurement of infrared emissivity as a function of frequency. Nicolet iS50 (Thermo Fisher, USA) equipment configured with a Pike gold mirror integrating sphere, an MCT liquid nitrogen detector, and a gold background was employed for that purpose. The measurement conditions consisted of a wavelength range of 2.5–15.3 μm, 64 scans, and scanning parameter of reflectivity or transmissivity with a resolution of 4.0.

## 3. Results and discussion

The SEM images of the CoFe$_2$O$_4$@SiO$_2$ microspheres are presented in Fig. 1a. The pristine CoFe$_2$O$_4$@SiO$_2$ showed diameters between 320 and 360 nm coated with homogeneous and thin SiO$_2$ shells. The electron beam could partly pass through the shell to reach the bulk of the microspheres. The shattered SiO$_2$ layer with a thickness of 20 nm can be

seen in the enlarged image of Fig. 1a. Sample S1 presented a gauzy nanoflower structure on CoFe$_2$O$_4$@SiO$_2$ microspheres with thin and gap characteristics (Fig. 1b). The thickness of ZAO nanoflowers increased as a function of the feeding ratio. By comparison, sample S2 (Fig. 1c) illustrated clearer nanoflower morphology with petals and increased thickness. The total diameter of the microspheres slightly rose. As shown in Fig. 1d, sample S3 exhibited a lamellar nanoflower structure thicker than that of S2, as well as a larger pore volume. In Fig. 1e, ZAO of S4 grew so fast that the nanoflower structure sunk and turned into nanoflake stacking on the microsphere surface as reactants concentration increased. Besides, the morphology of S4 looked less uniform than the others. Hence, regulating the feeding ratio could control the growth of ZAO crystalline to yield appropriate ZAO structure, conducive to fostering multi-reflection and absorption of microwaves. Accordingly, S3 was determined as the optimal sample, thereby used for further study.

The elemental state of the best sample S3 was determined by EDS. As shown in Fig. 1f, S3 revealed the presence of elements Zn, Al, O, Si, Fe, and Co, indicating the successful synthesis of ternary core-shell structure CoFe$_2$O$_4$@SiO$_2$@ZAO.

The morphologies of core-shell multilayered composites were further studied by TEM. Fig. 2a-b shows the three-layer core-shell structures with CoFe$_2$O$_4$, SiO$_2$, and ZAO ordered from the interior to the exterior. The outermost ZAO displayed a layered nanosheet, consistent with SEM analysis. The elemental mapping images in Fig. 2c–f revealed Zn, Al, O,
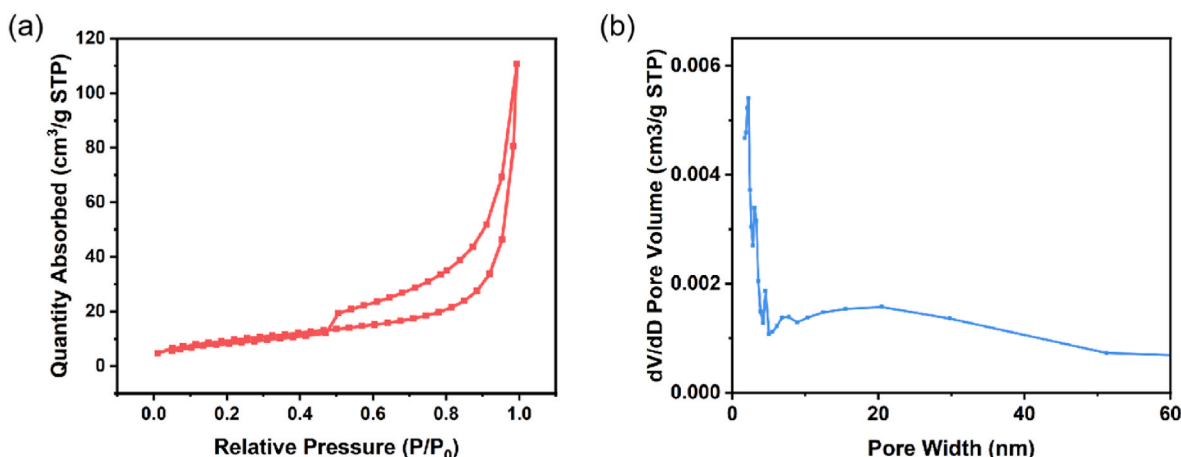


**Fig. 3.** (a) N$_2$ adsorption–desorption isotherm and (b) pore size distribution of sample S3.
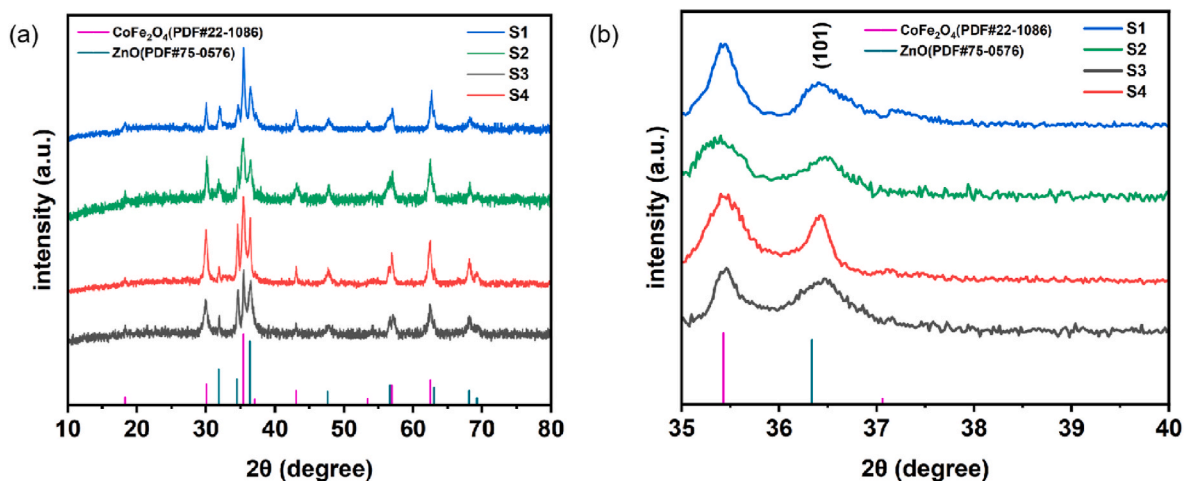
**Fig. 4.** (a) XRD patterns and (b) enlarged patterns of S1, S2, S3, and S4.
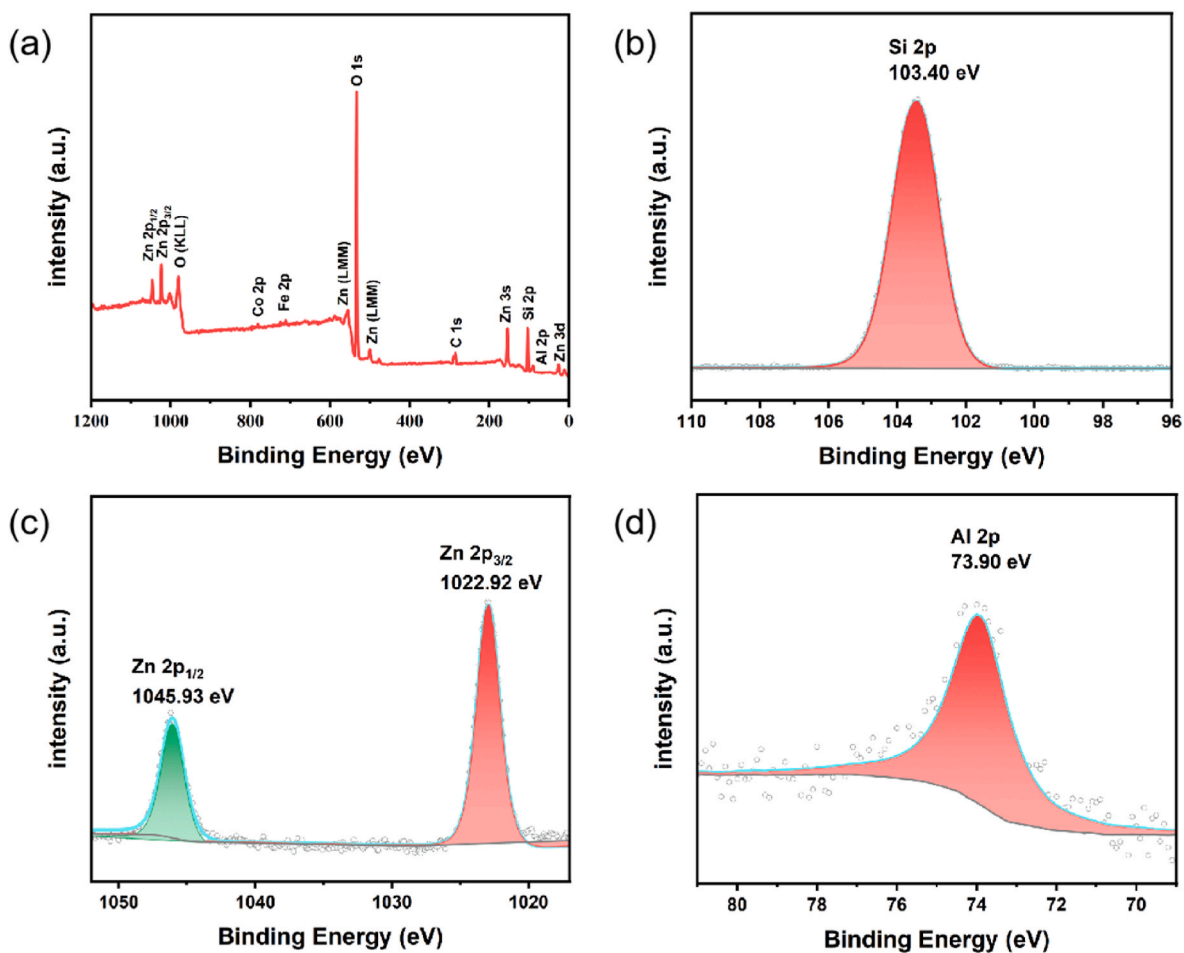


**Fig. 5.** (a) XPS survey spectrum of S3. High-resolution XPS spectra of (b) Si 2p, (c) Zn 2p, and (d) Al 2p.

Si, Fe, and Co elemental distributions consistent with the SEM mapping results, confirming the successful synthesis of the core-shell structure.

The $N_2$ adsorption curves of optimal sample S3 are provided in Fig. 3a. The profile showed isotherms between type III and type IV without adsorption inflection point in the low-pressure zone, namely no single-molecular adsorption layer relative to a material consisting of a macropore solid. The adsorption capacities sharply enhanced in the high-pressure range with no saturation plateau, consistent with the nanoflower multi-layer adsorption effect. As depicted in Fig. 1d, the optimal sample S3 featured an H3-type hysteresis loop with a large slope related to the adsorption and desorption branch, showing the presence of pores in the slit and layered nanoflower structure. According to the BJH model in Fig. 3b, S3 presented pores around 2.24, 3.05, 4.58, and 20.47 nm in size, with an average of 12.64 nm. Note that pore size may not only facilitate the multi-reflection but also enhance the scattering of electromagnetic waves and decline the infrared emissivity. The BET
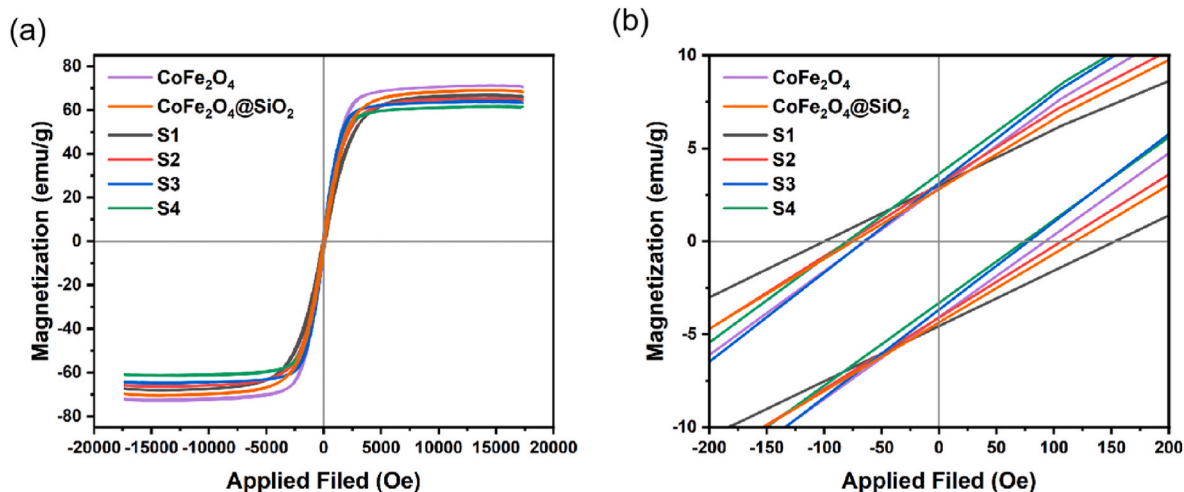
**Fig. 6.** (a) Magnetic hysteresis loops and (b) partial enlarged figures of CoFe$_2$O$_4$, CoFe$_2$O$_4$@SiO$_2$, S1, S2, S3, and S4.

**Table 2**
The $M_s$ and $H_c$ values of samples.

| Sample | $M_s$ (emu•g$^{-1}$) | $H_c$ (Oe) |
| --- | --- | --- |
| CoFe$_2$O$_4$ | 72.9 | 63.5 |
| CoFe$_2$O$_4$@SiO$_2$ | 70.5 | 74.1 |
| S1 | 68.1 | 99.8 |
| S2 | 66.5 | 78.8 |
| S3 | 64.9 | 65.0 |
| S4 | 61.4 | 79.2 |

surface area of S3 was determined as 234.43 m$^2$ g$^{-1}$. Such a high value was induced by the ZAO nano-flower structure. Meanwhile, the surfaces of nano-flowers may greatly boost the interface polarization effect under an electromagnetic field, thereby enhancing the microwave absorption characteristics.

The phase compositions and crystal structures of as-prepared samples were examined by XRD. As shown in Fig. 4a, highly crystalline samples were recorded. The crystal phase of CoFe$_2$O$_4$ spheres was further confirmed by XRD. In addition, the diffraction peaks at 2θ of 31.84°, 34.50°, 36.34°, 47.65°, 56.73°, 63.01°, and 68.12°, corresponding to (100), (002), (101), (102), (110), (103) and (112) crystal
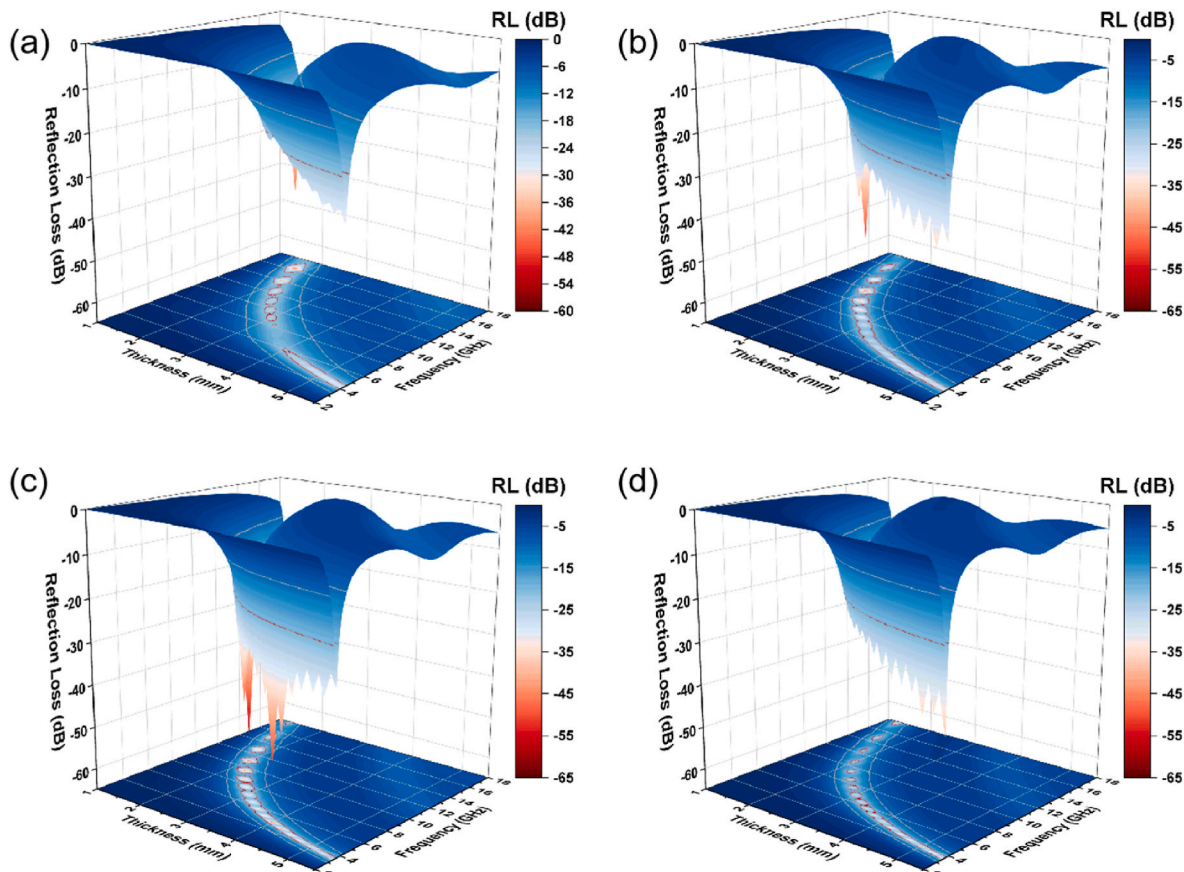


**Fig. 7.** Three-dimensional reflection loss images of (a) S1, (b) S2, (c) S3, and (d) S4.
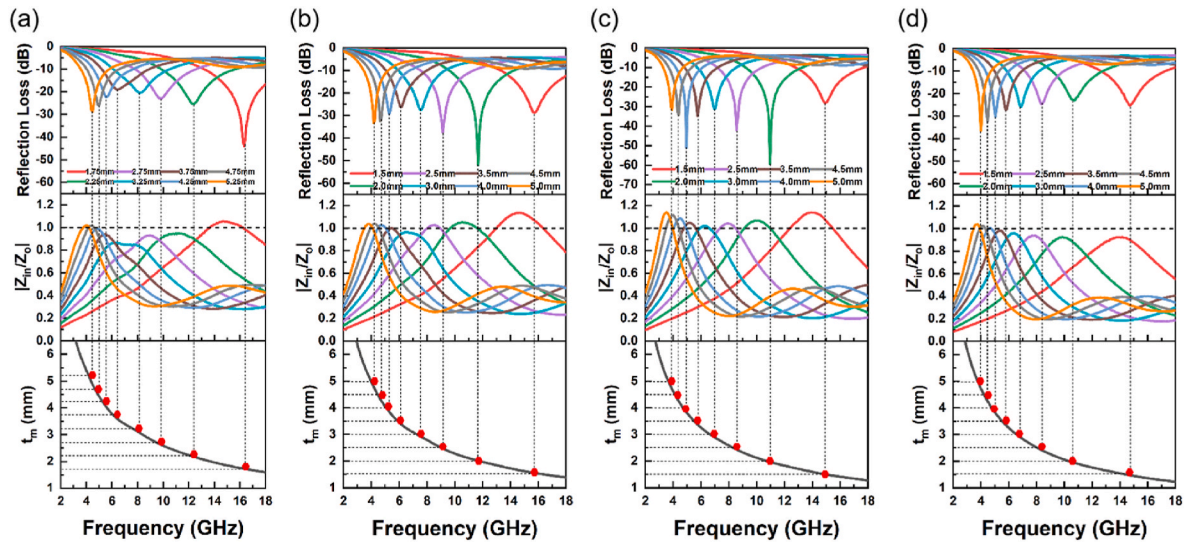
**Fig. 8.** Stack plots of two-dimensional reflection loss, impedance matching ($|Z_{in}/Z_0|$), and matching thickness ($t_m$) versus frequency of (a) S1, (b) S2, (c) S3, and (d) S4.

planes of ZnO (PDF#75–0576), respectively. All four samples showed consistent diffraction peak positions, with peak intensity strengthened as a function of ZAO content. In Fig. 4b, the position of (101) diffraction peak at 36.34° shifted toward higher angles. Hence, the incorporation of smaller Al atoms into the ZnO lattice resulted in shorter fringe spacing.

The oxidation states of the samples were confirmed by XPS. As shown in Fig. 5a, elements like Si, Zn, and Al were present in addition to Co, Fe, and O, consistent with EDS mappings and XRD results. The coexistence of the Si oxidation state in SiO$_2$ was evidenced by the shoulder observed on the main peak of 103.4 eV (Fig. 5b). The peaks at 1022.92 and 1045.93 eV in Fig. 5c corresponded to Zn 2p$_{3/2}$ and Zn 2p$_{1/2}$, respectively. The difference in binding energy between Zn 2p$_{3/2}$ and Zn 2p$_{1/2}$ was estimated to 23.04 eV, confirming the presence of Zn$^{2+}$ [22]. The inclusion of Al in the system shifted the Zn 2p$_{3/2}$ peak maximum from 1021.3 eV in standard oxide state to 1022.92 eV, accompanied by a decrease in Al 2p peak maximum (Fig. 5d) from 74.6 eV at standard status to 73.9 eV, demonstrating the presence of ZAO and the successful synthesis of the core-shell structure.

The effect of ZAO concentration on the magnetic characteristics of the core-shell structures was investigated by VSM. The hysteresis loops of CoFe$_2$O$_4$, CoFe$_2$O$_4$@SiO$_2$, and the four ternary samples (S1, S2, S3, S4) at 25 °C are compared in Fig. 6a. The addition of SiO$_2$ and ZAO gradually dropped the $M_s$, but all values were above 60 emu·g$^{-1}$. However, $H_c$ exhibited irregular variations (Fig. 6b), with the biggest $H_c$ value recorded with S1 and the smallest with both S3 and S4. The initial permeability ($\mu_i$) can be calculated according to Eq. (1) [29]:

$$\mu_i = \frac{M_s^2}{akH_cM_s + b\lambda\xi} \tag{1}$$

where $a$ and $b$ are material constants. $\lambda$ and $\xi$ represent the magneto-striction coefficient and elastic parameter, respectively.

Obviously, larger $M_s$ and smaller $H_c$ resulted in higher $\mu_i$. Among all four samples, S3 showed the largest $\mu_i$, conducive to enhancing the magnetic loss performance. The values of $M_s$ and $H_c$ are listed in Table 2.

The absorption properties were evaluated by calculating the reflection loss (RL) using the transmission line theory [30–34]:

$$Z_{in} = Z_0 \sqrt{\mu_r/\varepsilon_r} \tan h \left[ j(2\pi fd/c)\sqrt{\mu_r\varepsilon_r} \right] \tag{2}$$

$$RL = 20 \log |(Z_{in} - Z_0)/(Z_{in} + Z_0)| \tag{3}$$

where $Z_{in}$ and $Z_0$ represent the input characteristic impedance of

materials and the impedance of free space. $c$ is the speed of light in a vacuum, and $d$ refers to the thickness of the microwave absorber.

The RL$_{min}$ value of S1 with 1.75 mm thickness was recorded as −44.06 dB at 16.32 GHz (Fig. 7a). Meanwhile, the EAB was estimated to 4.8 GHz at 13.2–18 GHz. For bare CoFe$_2$O$_4$ microspheres, the RL$_{min}$ at 5.0 mm thickness achieved −17.51 dB at 6.12 GHz and EAB at 2.52 GHz (from 4.92 to 7.44 GHz). Both RL$_{min}$ and EAB of S1 looked significantly higher than those of CoFe$_2$O$_4$. Hence, the layers of SiO$_2$ and ZAO significantly affected the absorbing performance due to the introduction of dielectric loss and the improvement of wave multireflection from the shell.

As shown in Fig. 7b, the increase in ZAO content resulted in an RL$_{min}$ of −51.97 dB at 11.68 GHz and an EAB of 4.72 GHz, equivalent to changes from 9.52 to 14.24 GHz for sample S2. The RL$_{min}$ of S2 also increased at other matching thicknesses. Therefore, the rise in ZAO content introduced more dipole polarization effect, and the upsurge in the number and thickness of nano-petals expanded the multireflection space. As shown in Fig. 7c, S3 displayed the best absorption properties, with an RL$_{min}$ of −59.31 dB at 10.96 GHz for a thickness of 2 mm, as well as an EAB of 4 GHz (9.2–13.2 GHz). After reaching the maximum sheets size, ZAO nanoflower formed numerous holes, suitable for microwave reflection and enhancement of wave absorption.

Noticeably, the RL$_{min}$ of sample S4 diminished to −36.51 dB, resulting in an EAB of only 1.36 GHz. Also, the matching thickness of S4 rose to 5 mm (Fig. 7d). Since the collapse of the ZAO nanoflower structure left less interface and reflection space, the absorption qualities dramatically deteriorated. As ZAO increased, the frequency of RL$_{min}$ peak gradually shifted toward lower values, correlating to the same thickness. Meanwhile, the RL$_{min}$ at the lower frequency did not significantly decrease, consistent with a reduction in frequency of the RL$_{min}$ peak as a function of thickness (combination of the three-dimensional diagrams of the absorbing properties of all four samples). Consequently, the RL$_{min}$ peak shifted to the left owing to the increased wall thickness of ZAO nanoflowers.

The impedance matching and matching thickness of samples S1, S2, S3, and S4 are compared in Fig. 8. The RL$_{min}$ peak frequencies of all samples corresponded to the dashed line ($|Z_{in}/Z_0| = 1$), suggesting impedance matching as the primary factor affecting the absorption performance. The best impedance matchings were observed with S2 and S3 samples, showing optimal ZAO contents. The impedance mismatch of each sample was close to 1. Meanwhile, no severe impedance mismatch was noticed, suggesting excellent impedance matching of ZAO. The
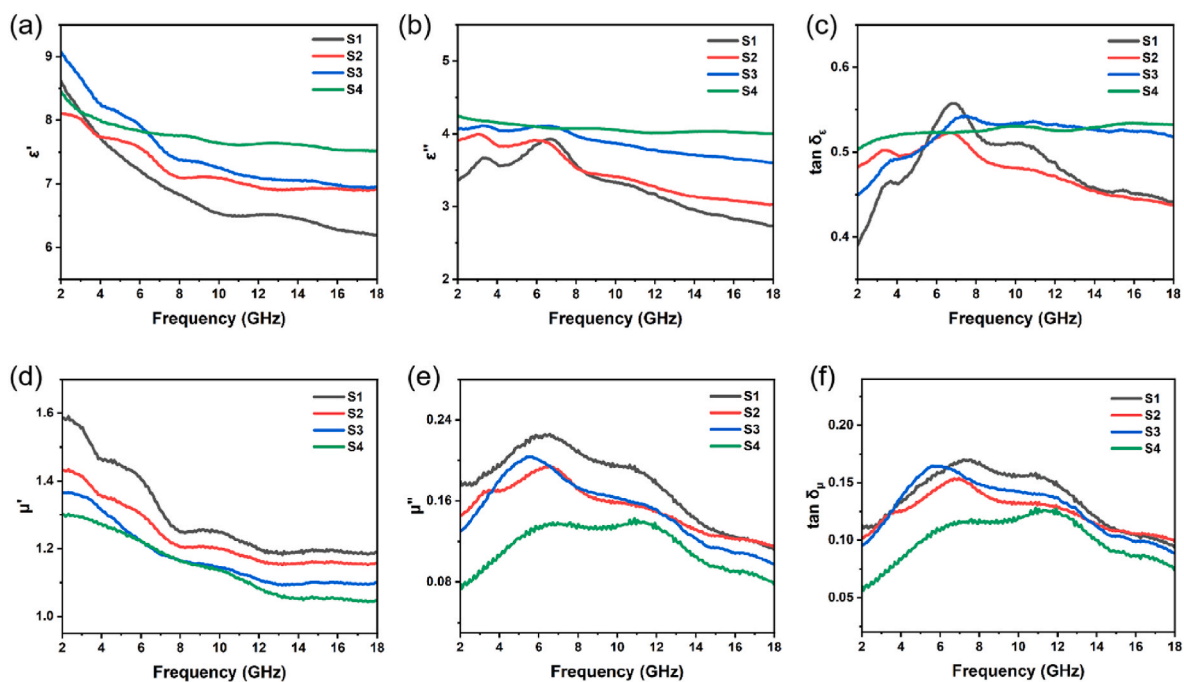
**Fig. 9.** (a) Real part of permittivity($\varepsilon'$), (b) imaginary part of permittivity($\varepsilon''$), (c) dielectric loss tangent (tan$\delta_\varepsilon$), (d) real part of permeability($\mu'$), (e) imaginary part of permeability($\mu''$), and (f) magnetic loss tangent (tan$\delta_\mu$) of S1, S2, S3, and S4.
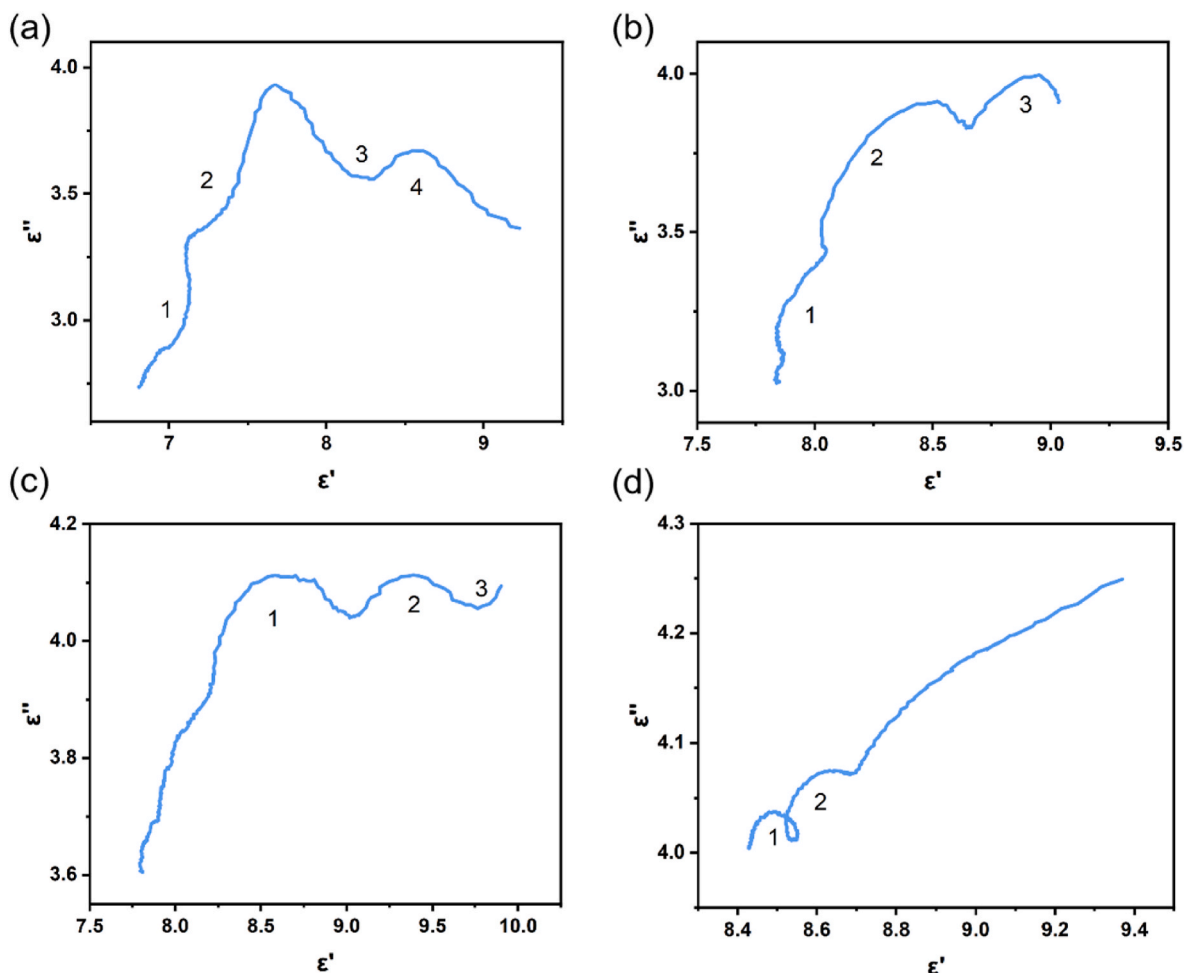


**Fig. 10.** Cole–Cole diagrams ($\varepsilon'$–$\varepsilon''$ curves) of (a) S1, (b) S2, (c) S3, and (d) S4.
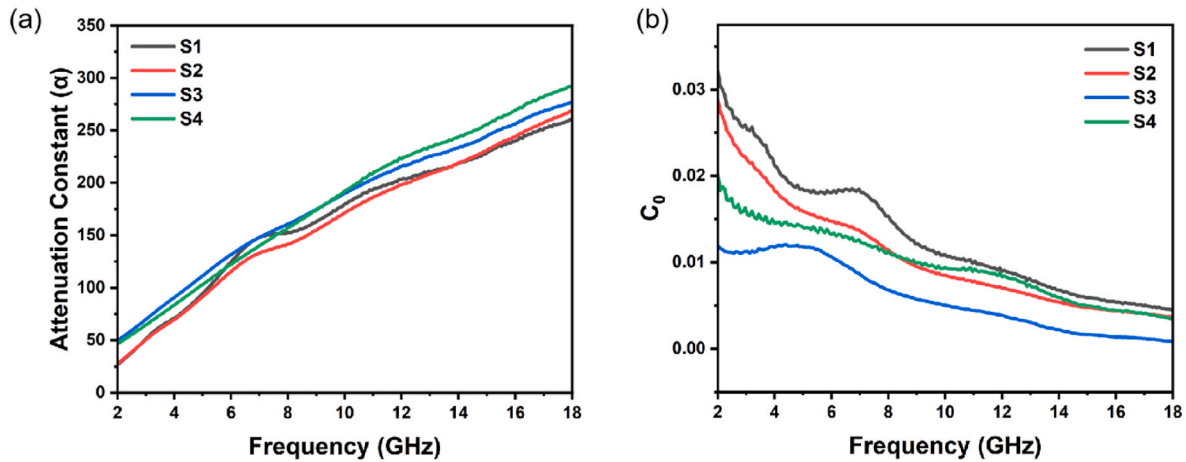
**Fig. 11.** (a) Eddy current loss coefficients and (b) attenuation constant (α) of S1, S2, S3, and S4.

matched thicknesses of all samples adhered to the 1/4 wavelength matching model. The relationship between matching thickness ($t_m$) and peak frequency ($f_m$) can be estimated by Eq. (4) [35–37]:

$$t_m = \frac{n\lambda}{4} = \frac{nc}{4f_m\sqrt{|\varepsilon_r||\mu_r|}} \quad (n = 1, 3, 5 \cdots) \tag{4}$$

The phase angles of electromagnetic wave incidence and reflection were analyzed for a wave absorber conform to the 1/4 wavelength matching model. In this case, the reflected electromagnetic waves from the interface lagged behind the incident electromagnetic wave by 180°, resulting in a significant interference effect and leading to high reflection loss performance.

To examine the impact of ZAO content on the electromagnetic properties of the materials, the relationship between the dielectric constant, magnetic permeability, and loss tangent was analyzed and the data are gathered in Fig. 9. Using $SiO_2$ and ZAO layers, the $\varepsilon'$ of all samples improved (Fig. 9a), confirming the influence of the carriers generated in ZAO. Also, higher ZAO concentrations resulted in a greater $\varepsilon'$ increase. In addition, the $\varepsilon'$ curve of S4 with the highest content of ZAO compared well with the other three samples, indicating that high enough ZAO proportion led to lower correlation between dielectric properties and $CoFe_2O_4$. The latter can also be confirmed in other parameters. The variation of $\varepsilon''$ versus frequency can be drawn according to Eq. (5) [38]:

$$\varepsilon'' = \varepsilon_r'' + \varepsilon_c'' = \frac{\varepsilon_s - \varepsilon_\infty}{1 + \omega^2\tau^2} + \frac{\sigma}{\omega\varepsilon_0} \tag{5}$$

where $\varepsilon_r''$ and $\varepsilon_c''$ represent the polarization loss and conductive loss, while $\varepsilon_s$, $\varepsilon_\infty$, $\sigma$, and $\tau$ correspond to the static dielectric constant, dielectric constant at infinite frequency, electrical conductivity, and polarization relaxation time, respectively [39,40].

In Fig. 9b, $\varepsilon''$ also rose with ZAO content owing to the greater number of carriers and additional losses, such as interface polarization and dipole polarization caused by $SiO_2$ and ZAO. Additionally, S1, S2, and S3 all exhibited relaxation resonance peaks at 6–8 GHz. Therefore, S4 did not possess a resonance peak due to nanoflower collapse, interface reduction, and other factors. In Fig. 9c, samples S3 and S4 depicted the strongest dielectric loss enhancement by the polarization loss of ZAO, implying ZAO as a major source of dielectric loss.

The Debye polarization relaxation was used to analyze the influence of dielectric loss and conductive loss during the absorbing process. Accordingly, the dielectric loss mechanism was divided into electron polarization, ion polarization, dipole polarization, and interface polarization. Recent studies showed the occurrence of both ion polarization and electron polarization at high frequencies. Therefore, the two main polarization mechanisms at 2–18 GHz were based on interface

polarization and dipole polarization. Debye relaxation theory can be expressed by Eq. (6) [41–43]:

$$\left(\varepsilon' - \frac{\varepsilon_s + \varepsilon_\infty}{2}\right)^2 + (\varepsilon'')^2 = \left(\frac{\varepsilon_s - \varepsilon_\infty}{2}\right)^2 \tag{6}$$

Accordingly, a semicircle relationship between $\varepsilon'$ and $\varepsilon''$ (Cole-Cole semicircle) would indicate the occurrence of the Debye relaxation process. Based on the literature [44], curves of $\varepsilon'$-$\varepsilon''$ showing a straight line would suggest conductive loss replacing the dielectric loss as the main loss mechanism [45,46]. The Cole-Cole diagrams for the four samples (S1, S2, S3, and S4) are presented in Fig. 10. All samples showed varying degrees of Debye polarization relaxation. As ZAO content increased, the number of Cole-Cole semicircles decreased with a linear correlation. Hence, the change in surface morphology reduced the relaxation phenomenon, such as interface polarization. Also, the increment in the number of carriers resulted in more conductive loss.

Here, the magnetic loss may be similar to previously used $CoFe_2O_4$ as the core in the same way [47]. The changes in $\mu'$ values as a function of frequency are presented in Fig. 9d. The increment in ZAO content led to a gradual decline in the magnetic component, resulting in the constant decrease of $\mu'$ values. Of note, the trend of $\mu''$ in Fig. 9e was theoretically related to the proportion of magnetic components, almost the same as that of $\mu'$. Compared to S4, sample S3 possessed larger $M_s$ and smaller $H_c$ values. As a result, the $\mu''$ representing the magnetic loss capacity was also higher than S4 but close to S1. The magnetic loss capacities reflected in $\tan\delta_\mu$ ($\tan\delta_\mu = \mu''/\mu'$) decreased in the following order: S1>S3>S2>S4. In general, modulating the coating of ZAO would improve the magnetic loss while gradually declining the extent of dielectric loss.

The attenuation constant (α) was used to evaluate the attenuation capacities of the as-prepared materials since it can be useful to determine the microwave absorption performance. This can be described by Eq. (7) [48]:

$$\alpha = \frac{\sqrt{2}\pi f}{c} \times \sqrt{(\mu''\varepsilon'' - \mu'\varepsilon') + \sqrt{(\mu''\varepsilon'' - \mu'\varepsilon')^2 + (\mu'\varepsilon'' + \mu''\varepsilon')^2}} \tag{7}$$

As shown in Fig. 11, the α values of four samples increased with frequency. The values of S3 and S4 samples were slightly higher than those of S1 and S2. Thus, it can be deduced that the increase in ZAO content led to partial loss of magnetic loss performance, while providing better dielectric loss properties. As a result, the α values of S3 and S4 were higher.

The occurrence of eddy current loss in the absorber resulted in a constant $C_0$ value versus frequency, which could be described by Eq. (8) [43,49]:
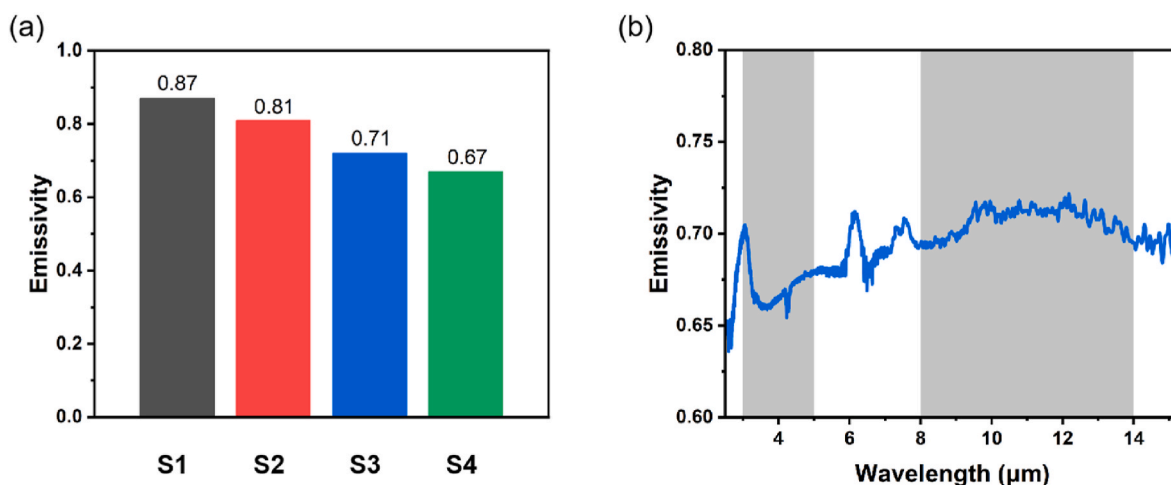
**Fig. 12.** (a) Average infrared emissivity of S1, S2, S3, and S4 at 8–14 μm. (b).Infrared emissivity versus frequency for S3 in the band of 2.5–15.3 μm.

$$C_o = \mu''(\mu')^{-2}f^{-1} = 2\pi\mu_0 d^2\delta \tag{8}$$

where $C_0$ represents the eddy current loss coefficient, $d$ is the diameter of the nanoparticle, and $\delta$ refers to the electrical conductivity.

The fluctuation in $C_0$ of all samples as a function of frequency is provided in Fig. 11b. The eddy current loss determined by the nature of the ferrite CoFe$_2$O$_4$ hardly existed. However, the hysteresis curves enclosing a certain area (Fig. 6b) demonstrated the presence of magnetic hysteresis loss in all samples. Therefore, the magnetic loss mechanism of the as-prepared samples was mainly derived from residual loss and magnetic hysteresis loss.

The infrared emissivity values of the samples at a wavelength of 8–14 μm were determined by an infrared emissometer (model IR-II). As shown in Fig. 12a, downward trends were recorded as a function of ZAO content. The infrared emissivity values of both S3($\varepsilon_{em,8-14}$ = 0.71) and S4 ($\varepsilon_{em,8-14}$ = 0.67) were almost the same as that of the pure ZAO observed in other studies. The correlation between infrared emissivity and both material composition and morphology can be analyzed from two aspects. First, the microstructure would greatly influence the infrared emissivity of powder materials with the following established order: sheet-like powder < grain-like powder < rod-like powder [50]. As displayed in Fig. 1, both S1 and S2 presented gauze-like nanoflower. Likewise, S3 possessed a thicker nanopetal and lamellar structure, while S4 nanoflowers collapsed and the ZAO packed on the microsphere surface as spheres and irregular sheets. Therefore, S3 possessed the most favorable morphology for reducing infrared emissivity. Another contributing factor had to do with the concentration and number of carriers. Since the Al-doping contents of as-synthesized samples were all set to 7%, the concentration of carriers should basically be the same. In Fig. 9a-b, the dielectric permittivity decreased with ZAO content linked to the number of carriers. Therefore, the rise in ZAO content gradually enhanced the number of carriers, resulting in declined infrared emissivity. After reaching a certain ZAO content, the decreasing rate of emissivity substantially slowed down to become close to that of pure ZAO. For comparison, the infrared emissivities of S3 at 2.5–15.3 μm are shown in Fig. 12b. The emissivity peaks of the curves at 3 μm, 6.2 μm, and 7.5 μm represented the infrared absorption of the atmosphere. The average infrared emissivities of S3 in the range of 8–14 μm were similar to those obtained by IR-II, whereas those in the range of 3–5 μm were estimated to be only 0.66–0.67. The lower infrared emissivity of ZAO formed as a result of ZnO lattice turning into an N-type semiconductor owing to the incorporation of Al. In this process, Al served as the donor atom to provide a free electron and generate carriers by replacing the Zn atom. Moreover, oxygen vacancies and interstitial Zn atoms of ZAO also provided free electrons, conducive to declining infrared emissivity as the

greater concentration of carriers. Overall, sample S3 showed lower infrared emissivity due to the layered nanoflower and more ZAO coating, leading to the best absorption properties. Although S4 possessed the lowest infrared emissivity, it may be hard to apply as bifunctional material owing to its worse absorption properties.

## 4. Conclusions

Novel CoFe$_2$O$_4$@SiO$_2$@ZAO core-shell composites were successfully synthesized by the hydrolysis and sol-gel methods. As the feeding ratio of ZAO increased, the morphology of ZAO changed from gauzy nanoflower to lamellar nanoflower until the structure collapsed. S3 with lamellar nanoflower was found the most suitable sample to reducing the infrared emissivity. The porous structure of S3 reached a BET surface area of 234.43 m$^2$ g$^{-1}$, conducive to enhancing the interface polarization and multireflection on electromagnetic waves. Additionally, the introduction of ZAO brought dipole polarization under alternating electric field, resulting in more loss mechanism. The RL$_{min}$ of S3 reached −59.31 dB at 10.96 GHz and 2 mm thick while EAB was 4 GHz (9.2–13.2 GHz). In the range of 8–14 μm, the infrared emissivity of CoFe$_2$O$_4$@SiO$_2$@ZAO decreased as a function of the increase in ZAO content. The average infrared emissivity of the best sample (S3) reached 0.71, realizing 0.66–0.77 in the waveband of 3–5 μm. Overall, CoFe$_2$O$_4$@SiO$_2$@ZAO ternary composites possess microwave absorption and low infrared emissivity, demonstrating the feasibility of producing dual-function materials with core-shell structure.

## Declaration of competing interest

The authors declare that they have no known competing financial interests or personal relationships that could have appeared to influence the work reported in this paper.

## Acknowledgments

## References

[1] T. Yang, X. Bai, D. Gao, L. Wu, B. Li, J. Thong, C. Qiu, Invisible sensors: simultaneous sensing and camouflaging in multiphysical fields, Adv. Mater. 27 (47) (2015) 7752–7758, https://doi.org/10.1002/adma.201502513.
[2] G. Song, C. Zhang, Q. Cheng, Y. Jing, C. Qiu, T. Cui, Transparent coupled membrane metamaterials with simultaneous microwave absorption and sound

reduction, Opt Express 26 (18) (2018) 22916–22925, https://doi.org/10.1364/OE.26.022916.

[3] D. Qi, X. Wang, Y. Cheng, R. Gong, B. Li, Design and characterization of one-dimensional photonic crystals based on ZnS/Ge for infrared-visible compatible stealth applications, Opt. Mater. 62 (2016) 52–56, https://doi.org/10.1016/j.optmat.2016.09.024.

[4] J. Zhang, R. Liu, H. Wang, Y. Zhang, C. Wang, J. Shi, Design, fabrication and characterization of a thin infrared-visible bi-stealth film based on one-dimensional photonic crystal, Opt. Mater. Express 9 (1) (2019) 195–202, https://doi.org/10.1364/OME.9.000195.

[5] L. Phan, W. Walkup, D. Ordinario, E. Karshalev, J. Jocson, A. Burke, A. Gorodetsky, Reconfigurable infrared camouflage coatings from a cephalopod protein, Adv. Mater. 25 (39) (2013) 5621, https://doi.org/10.1002/adma.201301472.

[6] L. Xiao, H. Ma, J. Liu, W. Zhao, Y. Jia, Q. Zhao, K. Jiang, Fast adaptive thermal camouflage based on flexible VO₂/Graphene/CNT thin films, Nano Lett. 15 (12) (2015) 8365–8370, https://doi.org/10.1021/acs.nanolett.5b04090.

[7] Y. Duan, H. Pang, X. Wen, X. Zhang, T. Wang, Microwave absorption performance of FeCoNiAlCr₀.₉ alloy powders by adjusting the amount of process control agent, J. Mater. Sci. Technol. 77 (2021) 209–216, https://doi.org/10.1016/j.jmst.2020.09.049.

[8] H. Pang, Y. Duan, L. Huang, L. Song, J. Liu, T. Zhang, X. Yang, J. Liu, X. Ma, J. Di, X. Liu, Research advances in composition, structure and mechanisms of microwave absorbing materials, Compos. B Eng. 224 (2021), 109173, https://doi.org/10.1016/j.compositesb.2021.109173.

[9] S. Mahulikar, H. Sonawane, G. Rao, Infrared signature studies of aerospace vehicles, Prog. Aero. Sci. 43 (7–8) (2007) 218–245, https://doi.org/10.1016/j.paerosci.2007.06.002.

[10] S.M. Zhong, W. Jiang, P. Xu, T. Liu, J. Huang, Y. Ma, A radar-infrared bi-stealth structure based on metasurfaces, Appl. Phys. Lett. 110 (6) (2017), 063502, https://doi.org/10.1063/1.4975781.

[11] J. Wang, C. Wan, Q. Tang, J. Xu, N. Xu, S. Yu, X. Wang, H. Tian, Hydrothermal synthesis of rGO/Al/CoFe₂O₄ with low infrared emissivity and strong microwave absorption, Ceram. Int. 49 (2023) 12814–12821, https://doi.org/10.1016/j.ceramint.2022.12.147.

[12] Y. Pang, Y. Li, M. Yan, D. Liu, J. Wang, Z. Xu, S.B. Qu, Hybrid metasurfaces for microwave reflection and infrared emission reduction, Opt Express 26 (9) (2018) 11950–11958, https://doi.org/10.1364/OE.26.011950.

[13] S. Zhong, L. Wu, T. Liu, J. Huang, W. Jiang, Y. Ma, Transparent transmission-selective radar-infrared bi-stealth structure, Opt Express 26 (13) (2018) 16466–16476, https://doi.org/10.1364/OE.26.016466.

[14] C. Zhang, X. Wu, C. Huang, J. Peng, C. Ji, J. Yang, Y. Huang, Y. Guo, X. Luo, Flexible and transparent microwave–infrared bi-stealth structure, Adv. Mater. Technol. 4 (8) (2019), 1900063, https://doi.org/10.1002/admt.201900063.

[15] Y. Ma, L. Shi, J. Wang, L. Zhu, Y. Ran, Y. Liu, J. Li, A transparent and flexible metasurface with both low infrared emission and broadband microwave absorption, J. Mater. Sci. Mater. Electron. 32 (2) (2021) 2001–2010, https://doi.org/10.1007/s10854-020-04967-3.

[16] H. Liu, H. Xing, R. Shi, X. Ji, Facial synthesis of Al@MnO₂ with enhanced microwave absorption and low infrared emissivity, J. Mater. Sci. Mater. Electron. 31 (2020) 18791–18802, https://doi.org/10.1007/s10854-020-04967-3.

[17] J. Li, Z. Xu, T. Li, D. Zhi, Y. Chen, Q. Lu, J. Wang, Q. Liu, F. Meng, Multifunctional antimony tin oxide/reduced graphene oxide aerogels with wideband microwave absorption and low infrared emissivity, Compos. B Eng. 231 (2022), 109565, https://doi.org/10.1016/j.compositesb.2021.109565.

[18] X. Zhang, L. Cai, Z. Xiang, W. Lu, Hollow CuS microflowers anchored porous carbon composites as lightweight and broadband microwave absorber with flame-retardant and thermal stealth functions, Carbon 184 (2021) 514–525, https://doi.org/10.1016/j.carbon.2021.08.026.

[19] P. Liu, Y. Wang, G. Zhang, Y. Huang, R. Zhang, X. Liu, X. Zhang, R. Che, Hierarchical engineering of double-shelled nanotubes toward hetero-interfaces induced polarization and microscale magnetic interaction, Adv. Funct. Mater. 32 (33) (2022), 2202588, https://doi.org/10.1002/adfm.202202588.

[20] C. Li, S. Ji, X. Jiang, G.I.N. Waterhouse, Z. Zhang, L. Yu, Microwave absorption by watermelon-like microspheres composed of γ-Fe₂O₃, microporous silica and polypyrrole, J. Mater. Sci. 53 (13) (2018) 9635–9649, https://doi.org/10.1007/s10853-018-2262-z.

[21] J. Wang, S. Hu, Q. Tang, J. Xu, N. Xu, S. Yu, X. Wang, H. Tian, One-pot hydrothermally prepared rGO/SiC/CoFe₂O₄ composites with strong microwave absorption at different thicknesses, Ceram. Int. 48 (20) (2022) 30640–30650, https://doi.org/10.1016/j.ceramint.2022.07.007.

[22] G. Cheng, F. Pan, X. Zhu, Y. Dong, L. Cai, W. Lu, Onion skin-derived hierarchical carbon/hollow CoFe₂O₄ composite with effective microwave absorption in multi-band, Compos. Commun. 27 (2021), 100867, https://doi.org/10.1016/j.coco.2021.100867.

[23] M. Rydzek, M. Reidinger, M. Arduini-Schuster, J. Manara, Low-emitting surfaces prepared by applying transparent aluminum-doped zinc oxide coatings via a sol–gel process, Thin Solid Films 520 (2012) 4114–4118, https://doi.org/10.1016/j.tsf.2011.04.105.

[24] T. Gurugubelli, B. Babu, J. Kim, K. Yoo, Efficient photoelectrochemical water oxidation and electrochemical supercapacitor performance of ZnAl₂O₄ hexagonal microstructures, Mater. Lett. 313 (2022), 131812, https://doi.org/10.1016/j.matlet.2022.131812.

[25] Y. Wang, F. Luo, L. Zhang, D. Zhu, W. Zhou, Microwave dielectric properties of Al-doped ZnO powders synthesized by coprecipitation method, Ceram. Int. 39 (2013) 8723–8727, https://doi.org/10.1016/j.ceramint.2013.04.056.

[26] Z. Du, D. Wang, X. Zhang, Z. Yi, J. Tang, P. Yang, R. Cai, S. Yi, J. Rao, Y. Zhang, Core-shell structured SiO₂/NiFe LDH composite for broadband electromagnetic wave absorption, Int. J. Mol. Sci. 24 (1) (2022) 504, https://doi.org/10.3390/ijms24010504.

[27] C. Gong, X. Wang, X. Zhang, X. Zhao, H. Meng, Y. Jia, J. Zhang, Z. Zhang, Synthesis of Ni/SiO₂ nanocomposites for tunable electromagnetic absorption, Mater. Lett. 121 (2014) 81–84, https://doi.org/10.1016/j.matlet.2014.01.138.

[28] B. Wang, Q. Wu, Y. Fu, T. Liu, Yolk-shell structured Co@SiO₂@Void@C nanocomposite with tunable cavity prepared by etching of SiO₂ as high-efficiency microwave absorber, J. Colloid Interface Sci. 594 (2021) 342–351, https://doi.org/10.1016/j.jcis.2021.03.011.

[29] M. Zhang, J. Qiu, Z. Xin, X. Sun, In situ reduced multi-core yolk-shell Co@C nanospheres for broadband microwave absorption, Materials 14 (16) (2021) 4610, https://doi.org/10.3390/ma14164610.

[30] J. Liu, J. Cheng, R. Che, J. Xu, M. Liu, Z. Liu, Double-Shelled yolk–shell microspheres with Fe₃O₄ cores and SnO₂ double shells as high-performance microwave absorbers, J. Phys. Chem. C 117 (1) (2012) 489–495, https://doi.org/10.1021/jp310898z.

[31] R. Che, L. Peng, X. Duan, Q. Chen, X. Liang, Microwave absorption enhancement and complex permittivity and permeability of Fe encapsulated within carbon nanotubes, Adv. Mater. 16 (5) (2004) 401–405, https://doi.org/10.1002/adma.200306460.

[32] H. Yu, T. Wang, B. Wen, M. Lu, Z. Xu, C. Zhu, Y. Chen, X. Xue, C. Sun, M. Cao, Graphene/polyaniline nanorod arrays: synthesis and excellent electromagnetic absorption properties, J. Mater. Chem. 22 (40) (2012) 21679–21685, https://doi.org/10.1039/c2jm34273a.

[33] J. Zheng, H. Lv, X. Lin, G. Ji, X. Li, Y. Du, Enhanced microwave electromagnetic properties of Fe₃O₄/graphene nanosheet composites, J. Alloys Compd. 589 (2014) 174–181, https://doi.org/10.1016/j.jallcom.2013.11.114.

[34] M. Meshram, N. Agrawal, B. Sinha, P. Misra, Characterization of M-type barium hexagonal ferrite-based wide band microwave absorber, J. Magn. Magn. Mater. 271 (2–3) (2004) 207–214, https://doi.org/10.1016/j.jmmm.2003.09.045.

[35] M. Qiao, X. Lei, Y. Ma, L. Tian, X. He, K. Su, Q. Zhang, Application of yolk–shell Fe₃O₄@N-doped carbon nanochains as highly effective microwave-absorption material, Nano Res. 11 (3) (2018) 1500–1519, https://doi.org/10.1007/s12274-017-1767-0.

[36] S. Wang, Y. Zhao, H. Xue, J. Xie, C. Feng, H. Li, D. Shi, S. Muhammad, Q. Jiao, Preparation of flower-like CoFe₂O₄@graphene composites and their microwave absorbing properties, Mater. Lett. 223 (2018) 186–189, https://doi.org/10.1016/j.matlet.2018.04.050.

[37] G. Shen, J. Ren, B. Zhao, B. Mei, H. Wu, X. Fang, Y. Xu, Magnetic hollow mesoporous carbon composites with impedance matching for highly effective microwave absorption, J. Mater. Sci. 54 (5) (2018) 4024–4037, https://doi.org/10.1007/s10853-018-3100-z.

[38] H. Zhang, B. Wang, A. Feng, N. Zhang, Z. Jia, Z. Huang, X. Liu, G. Wu, Mesoporous carbon hollow microspheres with tunable pore size and shell thickness as efficient electromagnetic wave absorbers, Compos. B Eng. 167 (2019) 690–699, https://doi.org/10.1016/j.compositesb.2019.03.055.

[39] Y. Du, W. Liu, R. Qiang, Y. Wang, X. Han, J. Ma, P. Xu, Shell thickness-dependent microwave absorption of core-shell Fe₃O₄@C composites, ACS Appl. Mater. Interfaces 6 (15) (2014) 12997–13006, https://doi.org/10.1021/am502910d.

[40] H. Lv, Z. Yang, P. Wang, G. Ji, J. Song, L. Zheng, H. Zeng, Z. Xu, A voltage-boosting strategy enabling a low-frequency, flexible electromagnetic wave absorption device, Adv. Mater. 30 (15) (2018), 1706343, https://doi.org/10.1002/adma.201706343.

[41] Z. Liao, M. Ma, Z. Tong, R. Wang, Y. Bi, Y. Chen, K. Chung, Y. Ma, Fabrication of ZnFe₂O₄/C@PPy composites with efficient electromagnetic wave absorption properties, J. Colloid Interface Sci. 602 (2021) 602–611, https://doi.org/10.1016/j.jcis.2021.06.042.

[42] L. Wang, X. Yu, X. Li, J. Zhang, M. Wang, R. Che, Conductive-network enhanced microwave absorption performance from carbon coated defect-rich Fe₂O₃ anchored on multi-wall carbon nanotubes, Carbon 155 (2019) 298–308, https://doi.org/10.1016/j.carbon.2019.07.049.

[43] X. Liang, Z. Man, B. Quan, J. Zheng, W. Gu, Z. Zhang, G. Ji, Environment-stable CoxNiy encapsulation in stacked porous carbon nanosheets for enhanced microwave absorption, Nano-Micro Lett. 12 (2020) 102, https://doi.org/10.1007/s40820-020-00432-2.

[44] Y. Duan, H. Pang, H. Zhang, Structure and composition design on ternary CNT@ZnFe₂O₄@ZnO composite utilized as enhanced microwave absorbing materials, Diam. Relat. Mater. 120 (2021), 108701, https://doi.org/10.1016/j.diamond.2021.108701.

[45] J. Wang, M. Zhou, Z. Xie, X. Hao, S. Tang, J. Wang, Z. Zou, G. Ji, Enhanced interfacial polarization of biomass-derived porous carbon with a low radar cross-section, J. Colloid Interface Sci. 612 (2022) 146–155, https://doi.org/10.1016/j.jcis.2021.12.162.

[46] X. Yang, Y. Duan, Y. Zeng, H. Pang, G. Ma, X. Dai, Experimental and theoretical evidence for temperature driving an electric-magnetic complementary effect in magnetic microwave absorbing materials, J. Mater. Chem. C 8 (5) (2020) 1583–1590, https://doi.org/10.1039/c9tc06551b.

[47] C. Wan, J. Wang, Z. Li, S. Yu, X. Wang, H. Tian, Optimized impedance matching and enhanced attenuation by heteroatoms doping of yolk-shell CoFe₂O₄@HCN as highly efficient microwave absorbers, Ceram. Int. 49 (2023) 21613–21623, https://doi.org/10.1016/j.ceramint.2023.03.297.

[48] H. Lv, G. Ji, X. Liang, H. Zhang, Y. Du, A novel rod-like MnO$_2$@Fe loading on graphene giving excellent electromagnetic absorption properties, J. Mater. Chem. C 3 (19) (2015) 5056–5064, https://doi.org/10.1039/c5tc00525f.

[49] M. Zeng, J. Liu, M. Yue, H. Yang, H. Dong, W. Tang, H. Jiang, X. Liu, R. Yu, High-frequency electromagnetic properties of the manganese ferrite nanoparticles, J. Appl. Phys. 117 (2015) 17B527, https://doi.org/10.1063/1.4917515.

[50] T. Guo, G. Xu, S. Tan, Z. Yang, H. Bu, G. Fang, H. Hou, J. Li, L. Pan, Controllable synthesis of ZnO with different morphologies and their morphology-dependent infrared emissivity in high temperature conditions, J. Alloys Compd. 804 (2019) 503–510, https://doi.org/10.1016/j.jallcom.2019.07.011.